Research Article

Nano Research
2023, 16(4): 5626–5639

ISSN 1998-0124 CN 11-5974/O4
https://doi.org/10.1007/s12274-022-5135-3

Local structure and magnetic properties of a nanocrystalline Mn-rich Cantor alloy thin film down to the atomic scale

Alevtina Smekhova[1] (✉), Alexei Kuzmin[2], Konrad Siemensmeyer[1], Chen Luo[1,3], James Taylor[1,3], Sangeeta Thakur[4], Florin Radu[1], Eugen Weschke[1], Ana Guilherme Buzanich[5], Bin Xiao[6], Alan Savan[6], Kirill V. Yusenko[5], and Alfred Ludwig[6]

[1] *Helmholtz-Zentrum Berlin für Materialien und Energie (HZB), Berlin D-12489, Germany*
[2] *Institute of Solid State Physics, University of Latvia, Riga LV-1063, Latvia*
[3] *Physik-Department, Technische Universität München, Garching D-85748, Germany*
[4] *Institut für Experimentalphysik, Freie Universität Berlin, Berlin 14195, Germany*
[5] *Bundesanstalt für Materialforschung und-prüfung (BAM), Berlin D-12489, Germany*
[6] *Institut für Werkstoffe, Ruhr-Universität Bochum, Bochum D-44801, Germany*

Received: 28 July 2022 / **Revised:** 20 September 2022 / **Accepted:** 29 September 2022

ABSTRACT

The huge atomic heterogeneity of high-entropy materials along with a possibility to unravel the behavior of individual components at the atomic scale suggests a great promise in designing new compositionally complex systems with the desired multi-functionality. Herein, we apply multi-edge X-ray absorption spectroscopy (extended X-ray absorption fine structure (EXAFS), X-ray absorption near edge structure (XANES), and X-ray magnetic circular dichroism (XMCD)) to probe the structural, electronic, and magnetic properties of all individual constituents in the single-phase face-centered cubic (fcc)-structured nanocrystalline thin film of $Cr_{20}Mn_{26}Fe_{18}Co_{19}Ni_{17}$ (at.%) high-entropy alloy on the local scale. The local crystallographic ordering and component-dependent lattice displacements were explored within the reverse Monte Carlo approach applied to EXAFS spectra collected at the K absorption edges of several constituents at room temperature. A homogeneous short-range fcc atomic environment around the absorbers of each type with very similar statistically averaged interatomic distances (2.54–2.55 Å) to their nearest-neighbors and enlarged structural relaxations of Cr atoms were revealed. XANES and XMCD spectra collected at the $L_{2,3}$ absorption edges of all principal components at low temperature from the oxidized and *in situ* cleaned surfaces were used to probe the oxidation states, the changes in the electronic structure, and magnetic behavior of all constituents at the surface and in the sub-surface volume of the film. The spin and orbital magnetic moments of Fe, Co, and Ni components were quantitatively evaluated. The presence of magnetic phase transitions and the co-existence of different magnetic phases were uncovered by conventional magnetometry in a broad temperature range.

KEYWORDS

high-entropy alloys, reverse Monte Carlo (RMC), element-specific spectroscopy, extended X-ray absorption fine structure (EXAFS), X-ray magnetic circular dichroism (XMCD), magnetism

1 Introduction

The design and comprehensive studies of multi-functional materials based on several d-block elements represent an actively developing field of modern materials science. Among various multicomponent systems, high-entropy and compositionally complex alloys together with high-entropy ceramics are already recognized as a promising class of functional materials [1–5] and exhibit their high potential and attractiveness for applications in renewable energy technologies [6]. In particular, high-entropy alloys (HEAs) formed by five or more principal components possess a high chemical complexity with a huge number of different local atomic configurations [7], which favour their remarkable performance in the areas of hydrogen storage [8, 9], carbon dioxide conversion [10], oxygen evolution and reduction [11, 12], in advanced nuclear applications [13], as noble-metal-free electrocatalysts [14, 15] and supercapacitors [16, 17]. At the same time, HEAs are known for their structural stability [18], enhanced mechanical properties [19–24], small diffusion mobility of atoms [7, 25], strength against corrosion [26–28], and improved radiation resistance [13, 29]. The equiatomic face-centered cubic (fcc) CrMnFeCoNi HEA—the so-called Cantor alloy—along with its modifications formed by non-equimolar compositions or different elemental compositions (e.g., isopleths of each constituent element [30, 31], a family of Cantor-Wu alloys [32, 33], or Al_xCrFeCoNi [27, 34–37]) are commonly considered as appropriate single-phase model systems that exhibit tailored properties and represent different high-entropy effects in compositionally complex compounds.

The key aspect of HEA local structure—a huge compositional complexity at the atomic level determined by a number of

Address correspondence to alevtina.smekhova@helmholtz-berlin.de

principal components—is the foundation of their diverse macroscopic properties. Lattice distortions [38–46], valence electron concentration [47], a possibility to form locally ordered structures [48, 49], magnetic moments of components along with their relative couplings [33, 37, 40], and component-specific structural displacements [37, 46, 50, 51] are already demonstrated to be important in explanations of HEAs macroscopic behavior and are in correlation with the microscopic phases. The attempts to understand and find out the roles of individual components in the properties of high-entropy systems as a whole were made both by theoretical calculations and experiments.

To effectively probe the peculiarities of the local coordination, electronic structure, and magnetic properties of a certain element in HEAs depending on the composition and preparation conditions, element-specific techniques based on X-ray absorption spectroscopy (XAS) at the absorption edges of principal components can be used. Multi-edge XAS studies performed at the synchrotron radiation large-scale facilities along with a proper data evaluation and interpretation can identify specific properties that are characteristic to the atomic scale, significantly complementing laboratory methods like X-ray diffraction (XRD), transmission/scanning electron microscopy (TEM/SEM), energy dispersive X-ray analysis (EDX), atomic probe tomography (APT), X-ray photoelectron spectroscopy (XPS), conventional magnetometry, as well as neutron diffraction characterization. Up to now, XAS studies with X-rays of variable polarization and tunable over the absorption edges energies in the hard or soft energy ranges are still underrepresented in the case of HEAs, and there are only a few examples involving the extended X-ray absorption fine structure (EXAFS) [37, 46, 50–52], X-ray absorption near edge structure (XANES) [33, 37, 51, 52], and X-ray magnetic circular dichroism (XMCD) techniques [33, 37]. In several cases of Fe-containing systems, Mössbauer spectroscopy with the use of non-polarized hard X-rays from a laboratory source was also effectively applied to HEAs [53] and high-entropy oxides [54].

Recently, we demonstrated the advantages of the element-specific EXAFS technique used in conjunction with the reverse Monte Carlo (RMC) based analysis to reveal individual atom pair distribution functions (PDFs) on the local scale up to several coordination shells in $Al_xCrFeCoNi$ [37] and equiatomic Cantor alloy [51]. For both systems, the statistically averaged interatomic distances between 3d absorbing atoms and their nearest-neighbors in the first coordination shell as well as quantitative estimations of component-dependent crystallographic lattice relaxations were found. Atomistic simulations performed within the RMC approach were used to overcome the well-known drawbacks of the conventional multi-shell fitting EXAFS analysis in the case of multicomponent materials such as HEAs: In the case when individual EXAFS spectra are fitted independently, a large number of fitting parameters and strong correlation between them could lead to unreliable and strongly biased results. Contrary to this, within the RMC approach, there is the possibility to simultaneously fit one and the same structural model to several experimental EXAFS spectra taken at the X-ray absorption edges of different constituents. The starting atomic configuration is constructed based on the known crystallographic structure and accounting for unit cell parameters, density, and atomic composition of the system. As a result of several RMC fits with a different local compositional disorder, a self-consistent structural model of the investigated HEA can be obtained through averaging over several final configurations of atoms. The fit performed in the wavelet space (i.e., in both *k* and *R* spaces) allows us to consider all subtle changes regarding both atom positions and their scattering amplitudes. Thus, the final model describes the independent sets of experimental EXAFS data with high accuracy. Accordingly, the obtained PDFs associated with the local crystallographic configurations of each constituent element make it possible to extract statistically averaged values of interatomic distances around absorbers of each type and local lattice displacements related to a particular type of atoms in the most unbiased manner. However, some natural limitations of the method do not allow one to make conclusions about possible short-range ordering effects in the case of systems that comprise neighboring elements in the periodic table [37, 51], despite the methodology itself being adapted to studies of the short-range order in different bimetallic nanocatalysts [55, 56].

XANES/XMCD studies are known to be useful in revealing the oxidation states, the chemical shifts of the absorption edges, and magnetic moments of individual components in various complex systems [57]. They can be applied to explore each of the 3d principal components at the surface of HEAs not only for bulk alloys with well-documented crystal structures but also for nanocrystalline powders and thin films which cannot be studied using X-ray diffraction. Specifically, XANES/XMCD spectra recorded at the $L_{2,3}$ absorption edges of the constituent elements of a HEA can provide evidence about peculiarities of the electronic states including a possible charge transfer [33, 52] for a particular component, along with its spin and orbital magnetic contributions to the total net magnetic moment [33, 37]. The latter quantities bring complementary information unattainable by conventional magnetometry, while serving as a more precise probe of the magnetic properties of surface elements that contribute significantly to, for example, catalytic performance. Since the macroscopic magnetic properties of HEAs strongly depend on their composition, crystallographic structure, and the preparation route [34, 37, 58, 59] leading to different microstructures, an even more complex picture of magnetic interactions is expected for the elements at the surface and in the sub-surface volume. When combined with surface treatments aimed at oxide reduction or with surface nanostructuring methods, XANES/XMCD studies would enable a deeper understanding of the impact of high-entropy mixing at low dimensions.

Herein, we employ EXAFS, XANES, and XMCD techniques to probe structural, electronic, and magnetic properties of the 3d-element constituents of a Mn-rich single-phase fcc CrMnFeCoNi nanocrystalline thin film in an element-specific manner and at the atomic scale. The multi-edge EXAFS analysis was done using the RMC method involving a simultaneous fit of the same structural model to EXAFS spectra collected at the K absorption edges of Cr, Fe, Co, and Ni at room temperature (RT). The extracted PDFs related to each principal component of the alloy were further used to confirm the short-range crystallographic structure and its homogeneity over the entire volume of the film for all constituents, to reveal the statistically averaged interatomic distances from absorbers of each type to their nearest-neighbors in the first coordination shell, and to evaluate the component-dependent lattice displacements. XANES/XMCD studies were performed at the $L_{2,3}$ absorption edges of each constituent at low temperature on the oxidized and *in situ* cleaned surfaces of the HEA film to probe the initial oxidation states and possible magnetic moments of surface ions, the changes caused by the surface treatment, and spin/orbital magnetic contributions to the total magnetic moment of a particular 3d constituent of the high-entropy alloy at the oxide-free surface. Conventional magnetometry was used to highlight the complex magnetic behavior of the entire volume of HEA film within a broad temperature range.

2 Experimental

2.1 Sample preparation and initial characterization

The Cantor alloy thin film Cr-Mn-Fe-Co-Ni (1,000 nm) was prepared in a loadlock-equipped ultra high vacuum (UHV) physical vapor deposition (PVD) co-sputter system (CMS 600/400 LIN, DCA Instruments, Finland) at Ruhr-University Bochum. The deposition chamber used had five magnetron sputter sources in a confocal arrangement spaced 72° apart, with Ø100 mm elemental targets of Cr (99.99%, Kaistar, USA), Mn (99.95%, Sindlhauser Materials, Germany), Fe (99.99%, Sindlhauser Materials, Germany), Co (99.99%, Sindlhauser Materials, Germany), and Ni (99.995%, K.J. Lesker, USA). The substrate was a (100)-oriented Si single crystal with 1,500 nm wet thermal SiO_2 as a barrier layer against reactions with the deposited film. The base pressure was 2×10^{-5} Pa and the depositions were done at a heater temperature of 25 °C without additional intentional heating. Uniformity of the film composition was achieved by using a substrate table rotation of 25 rpm. All targets were precleaned by sputtering against individual closed shutters immediately prior to the film deposition. Depositions were done at a working pressure of 6.7×10^{-1} Pa in pure Ar (99.9999%). The power applied to each cathode was adjusted to yield the desired film composition, with a resulting total deposition rate of 0.24 nm·s^{-1}.

The film was firstly characterized using XRD (Cu Kα radiation, λ = 1.5418 Å) in Bragg–Brentano geometry with a Johansson monochromator at room temperature. The XRD pattern (Fig. 1) demonstrates only one distinct and significantly broadened peak over the halo, pointing to the nanocrystalline structure of the film. As it will be further clarified by EXAFS in Section 3, the considered film exhibits evidence of the fcc local coordination for atoms of each type. Thus, the angular position of the main peak was assigned to the fcc lattice ($Fm\bar{3}m$ space group) with the unit cell parameter a = 0.3582 nm. The characteristic sizes of the nanocrystallites were estimated to be on the order of several nm.

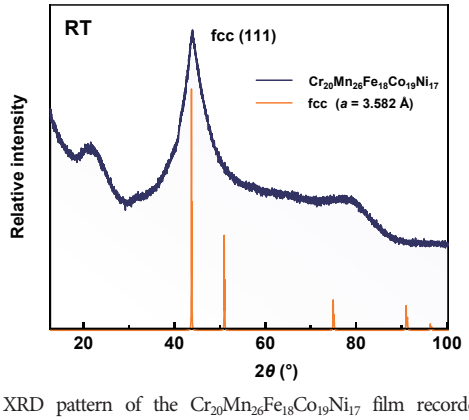

Figure 1 XRD pattern of the $Cr_{20}Mn_{26}Fe_{18}Co_{19}Ni_{17}$ film recorded at RT compared with the peak positions from the ideal fcc system of the same composition.

The composition of the as-prepared sample was determined as $Cr_{20}Mn_{26}Fe_{18}Co_{19}Ni_{17}$ (in at.%) using energy-dispersive X-ray spectroscopy (EDS, INCA, Oxford Instruments, UK) in a scanning electron microscope (5800LV, JEOL, Japan) operated at 20 kV, 600× magnification, working distance of 10 mm, and calibrated with a Co standard. A piece of bulk equiatomic Cr-Mn-Fe-Co-Ni alloy was used as an EDS calibration standard, which was certified using inductively coupled plasma (ICP) analysis.

Before X-ray diffraction, X-ray absorption spectroscopy, and magnetometry studies presented herein, the film was kept under ambient conditions for several months, which resulted in surface oxidation.

2.2 X-ray absorption spectroscopy at the K absorption edges

EXAFS spectra (Fig. 2) were recorded at the K absorption edges of Cr (5.99 keV), Fe (7.11 keV), Co (7.71 keV), and Ni (8.33 keV) by measuring fluorescent yield (FY) at the BAM*line* [60] of BESSY II synchrotron radiation facility operated by Helmholtz-Zentrum Berlin (HZB). The measurements were carried out with horizontally polarized hard X-rays from a 7 T wavelength shifter (WLS) at 21–22 °C in air. The film was fixed in the X-ray beam between two 50-μm thick Kapton foils. A custom-made four-element energy-dispersive detector was used to collect the fluorescence signal in a similar way as in Ref. [61].

2.3 RMC method

The RMC method makes it possible to fit one and the same structural model simultaneously to several EXAFS spectra collected at the X-ray absorption edges of the main components constituting a multicomponent system [37, 51]. Here, we used the RMC method as implemented in the EvAX code [62, 63]. It is based on the evolutionary algorithm (EA) for the acceleration of the optimization procedure [63] and uses the wavelet transforms (WTs) for the comparison between the experimental and calculated EXAFS spectra simultaneously in k and R spaces [64].

The structural model of the material is represented by a simulation box constructed as a supercell based on a repeating unit cell, which in turn can be obtained from X-ray diffraction data. The periodic boundary conditions (PBC) are imposed to avoid surface-related effects. The number of atoms in the simulation box is given by the density of the material. During the RMC simulation, the volume and the shape of the simulation box remain fixed, while the atoms are displaced randomly around their initial positions to account for the thermal and static disorders. The configuration-averaged (CA) EXAFS spectrum is then calculated over all absorbing atoms located in the simulation box using the multiple-scattering (MS) formalism. At each step of the RMC simulation, the difference between WTs of the experimental and CA-EXAFS spectra is evaluated and used for the optimization of the structural model [62, 63].

The main advantage of the RMC method as compared to conventional multi-shell EXAFS analysis becomes evident when the region around the absorbing atom contributing to the EXAFS spectrum extends up to distant coordination shells. In this case, the conventional approach will require the use of a huge number of model parameters due to the rapidly increasing number of scattering paths, which is usually overcome by introducing additional assumptions and restrictions on the interdependences between the parameters [65]. On the contrary, at each step of the RMC simulation, the CA-EXAFS spectrum is uniquely determined by the coordinates of atoms in the simulation box and can be accurately evaluated taking the MS effects into account. This allows one to account for the contributions from distant and overlapping coordination shells in the most unbiased manner. In this work, RMC simulations were applied to EXAFS spectra collected at the K absorption edges of four constituents (Cr, Fe, Co, and Ni).

The initial structural model was constructed in a form of the simulation box (Fig. 3) with a size of $4a \times 4a \times 4a$ employing the PBC with the experimental value of the lattice parameter a = 3.582 Å obtained by XRD. The Cr, Mn, Fe, Co, and Ni atoms (totally 256) were randomly distributed in a proper concentration (50 Cr, 67 Mn, 46 Fe, 49 Co, and 44 Ni) at the Wyckoff positions of the fcc lattice. The size of the simulation box was kept constant

during the RMC simulations. The number of atomic configurations simultaneously considered in the EA algorithm was 32 [63].

In the current study, we followed the same procedure as described previously in Refs. [37, 51]; the fixed simulation box size and small value of the largest permissible atom displacements (0.4 Å) play the role of constraints and stabilize the structural model. As a result, the final structural model does not deviate significantly from the chosen crystallographic structure while it takes into account and can describe both thermal and static disorders present in the alloy.

At each RMC iteration, the configuration-averaged K-edge EXAFS spectra $\chi(k)k^2$ were calculated over all Cr, Fe, Co, and Ni atoms (Fig. 4) in the constructed simulation box, and their Morlet WTs were compared with those of the experimental EXAFS spectra. The best agreement between the WTs of the experimental and calculated EXAFS spectra was used as a criterion for the model structure optimization. The experimental EXAFS spectra $\chi(k)k^2$ were extracted from the raw data using a conventional procedure [65] implemented in the XAESA code [66].

The WTs calculations were performed in the *k*-space range from 3.8 to 7.8 Å^{-1} for Cr and from 3.0 to 9.0 Å^{-1} for Fe, Co, and Ni; in the *R*-space the calculations were done in the range from 1.0 to 6.0 Å for all constituents. The number of RMC iterations was 5,000 to guarantee the convergence of the structural model; no significant improvements in the residuals were observed beyond this number. As a result of each RMC simulation, a set of atomic coordinates was obtained, which was further used to calculate the PDFs $g(r)$ (Fig. 5), the mean interatomic distances r, the mean square relative displacements (MSRDs) for each pair of atoms, and the mean square displacements (MSDs) for atoms of each type. To improve statistics, 12 sets of different (independent) starting structural models were considered for final PDFs.

During the RMC simulations, the CA-EXAFS spectra were calculated for atoms of each type (all constituents) using *ab initio* real-space multiple-scattering FEFF8.50L code [67, 68] including the MS effects up to the fourth order. More details about the simulations can be found in Ref. [51].

2.4 Magnetometry

Magnetometry measurements were carried out using a commercial magnetic properties measurement system (MPMS, Quantum Design) in magnetic flux densities up to 7 T at temperatures of 5–380 K (Fig. 6). The temperature dependences were recorded with and without applied magnetic fields. The field-assisted cooling (FC) in ±2 T was followed by the measurements of magnetic hysteresis loops without additional setting of the magnetic field to zero. The vibrating sample magnetometer (VSM) mode was used with a 14 Hz frequency and 2 mm amplitude. The sample was mounted within a plastic straw at approx. 45° with respect to the magnetic field direction. The total mass of the sample (18.25 mg) was measured with a microbalance; the mass of the $Cr_{20}Mn_{26}Fe_{18}Co_{19}Ni_{17}$ film was further estimated through the film thickness and composition (0.124 mg).

2.5 X-ray absorption spectroscopy at the $L_{2,3}$ absorption edges

XANES and XMCD spectra (see Figs. 7 and 8) were collected at the $L_{2,3}$ absorption edges of Cr (560–640 eV), Mn (630–670 eV), Fe (690–740 eV), Co (770–820 eV), and Ni (840–890 eV) at the high-field diffractometer end-station of the UE46_PGM-1 beamline [69, 70], also at BESSY II synchrotron radiation facility. X-ray absorption spectra for XANES and XMCD studies were recorded with linear and/or circular soft X-rays from the third harmonic of the elliptical undulator, respectively, in the total electron yield (TEY, drain current) detection mode. TEY of the Pt-coated Si mirror before the end-station was used for the normalization relative to the intensity of the incoming X-ray photons. XANES spectra were also collected at the O K absorption edge (520–570 eV) with linearly polarized X-rays; the measurements at the Cr $L_{2,3}$ edges and the O K edge were done without vacuum protective windows of the beamline. XMCD spectra were collected by alternating the X-ray beam helicity under an applied magnetic field of +4 T along the incident beam direction. The film was mounted in 45° incidence geometry. Element-specific hysteresis loops were recorded at particular energies in the ±0.5 T field range with a 0.0013 T·min^{-1} sweep rate (Fig. 9). Due to the sensitivity of the secondary electrons to the external magnetic fields, the most stable TEY signal from the sample can be collected under an application of magnetic fields above a certain threshold, below which a TEY instability region at smaller magnetic fields is present.

XANES/XMCD experiments with the *in situ* cleaned HEA film were performed at the recently installed VEKMAG end-station of the PM2 beamline at BESSY II [71]. The absorption spectra were recorded using circularly polarized X-rays from a bending magnet in TEY (drain current) detection mode, while flipping the magnetic field applied along the primary beam between ±4 T (Fig.10). The experiments were done at 10 K in the same 45° incidence geometry. The detected signal was normalized with respect to the incoming X-ray photons intensity measured by a Ta-coated mesh upstream of the end-station. Before the measurements, the sample was cleaned by Argon sputtering at 1 keV potential (~ 15–16 mA emission current) and 45° incidence for 80 min. The element-specific hysteresis loops were measured in a magnetic field range of ±4 T, where the sweep rate of the magnetic field was 2 T·min^{-1} (Fig. 11).

3 Results and discussion

3.1 EXAFS spectroscopy and RMC analysis

Element-specific X-ray absorption spectroscopy applied at the K absorption edges of Cr, Fe, Co, and Ni was used to probe the local environment of 3d constituent elements in the entire volume of the Mn-rich $Cr_{20}Mn_{26}Fe_{18}Co_{19}Ni_{17}$ thin film. X-ray absorption spectra recorded at RT are shown in Fig. 2 and represent the local coordination of a particular type of atoms in the alloy. The shape and positions of EXAFS oscillations found above each absorption edge indicate a dominantly homogeneous short-range (local) environment of Cr, Fe, Co, and Ni absorbers in the fcc lattice. The suppressed oscillations found above the Cr K-edge suggest the presence of local disorder caused by larger displacements of Cr atoms from their equilibrium positions or larger variations in their local environment as compared to Fe, Co, and Ni constituents. The possible contributions from the sub-surface oxidized atoms to the collected EXAFS spectra are negligible due to the large probing depth of FY detection mode.

As it was previously shown in Refs. [37, 51], a qualitative comparison of the collected EXAFS spectra with those for reference foils leads to the conclusion that the majority of atoms in the Cantor alloy film are integrated into the fcc HEA lattice independently of the crystal structure of the pure elements. The subsequent quantitative analysis was performed within the RMC approach that was used to overcome the drawbacks of the common multi-shell EXAFS analysis for multicomponent systems and to uncover the peculiarities of the nearest-neighbor distributions around a particular type of absorber at the atomic scale.

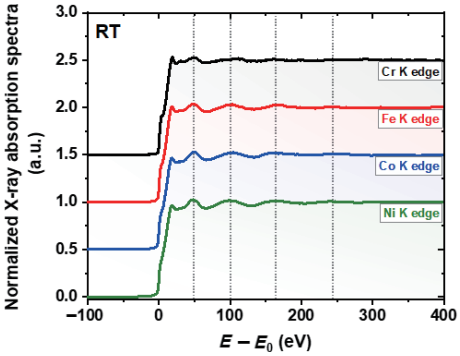

Figure 2 X-ray absorption spectra of the $Cr_{20}Mn_{26}Fe_{18}Co_{19}Ni_{17}$ film recorded at the K absorption edges of Cr (E_0 = 5,987 eV), Fe (E_0 = 7,112 eV), Co (E_0 = 7,709 eV), and Ni (E_0 = 8,333 eV) at RT using fluorescence yield. E_0 was determined as the energy corresponding to the first maximum of the first derivative of each spectrum. Spectra are normalized to unity and shifted vertically for clarity.

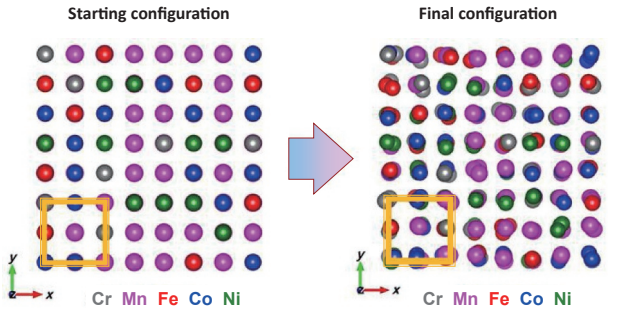

Figure 3 Examples of starting (initial) and final atom configurations (simulation boxes) used in the RMC simulations for simultaneous fit to EXAFS spectra of the $Cr_{20}Mn_{26}Fe_{18}Co_{19}Ni_{17}$ film at four (Cr, Fe, Co, and Ni) K absorption edges. The initial simulation box was randomly filled with atoms according to the film composition; periodic boundary conditions were applied. Colour scheme: Cr (gray), Mn (magenta), Fe (red), Co (blue), and Ni (green). The top views of both simulation boxes are shown along the *z*-direction in chosen *xyz* coordinates as depicted in the figures. The schematic border of the fcc unit cells is displayed at the bottom left of each figure.

One example of the initial and final configurations of atoms used in the RMC simulations is shown in Fig. 3. The particular structural model was simultaneously fitted to EXAFS spectra recorded at four absorption edges to find the coordinates of all relaxed atoms in the constructed simulation box. The obtained atomic coordinates were used to calculate total and partial element-specific PDFs. The EXAFS calculations were carried out within the multiple-scattering formalism including the scattering paths up to the fourth order. Note that the displacements of atoms in the final configuration account for both thermal and structural (radial and angular) disorders. This approach allows performing a reliable analysis of the available experimental EXAFS data in the most unbiased manner and reconstructing the local environment in the first five coordination shells around each of the 3d absorbers (distances up to ~ 6.0 Å) even in the absence of the EXAFS data for one constituent element. In the current case, the Mn K-edge data have not been considered due to their limited quality.

The experimental and RMC-fitted k^2-weighted EXAFS spectra $\chi(k)k^2$, and their Fourier and wavelet transforms are shown in Fig. 4. A good agreement between the experimental and RMC-fitted data is seen in both *k*- and *R*-spaces at all considered K-edges. This suggests that the single structural model, based on randomly distributed atoms according to the film composition, can reproduce the experimental EXAFS spectra with high accuracy. Accordingly, the obtained final configuration of atoms is supposed to represent the most valuable arrangement of the nearest-neighbors in the first coordination shell of the corresponding 3d absorber with high precision. For the fcc lattice, the configuration of atoms in the first coordination shell is mainly responsible for the first peak in Fourier transforms (FTs) located in the range from 1.0 to 3.0 Å.

The atomic coordinates of the final structural models obtained from 12 independent simulations were used to calculate the total and partial PDFs shown in Fig. 5. Each of these PDFs is an element-specific projection of the three-dimensional structure of a material over a radial distance relative to the chosen absorbing atom and represents the amount and the type of atoms located at a particular distance from the absorber. Since the simultaneous fit to four independent experimental EXAFS spectra collected at different absorption edges is going in the wavelet space, it automatically takes into account the small differences in the scattering amplitudes of 3d constituents and guarantees a proper accounting of the contributions from all principal components. The total PDFs averaged over each pair of five different

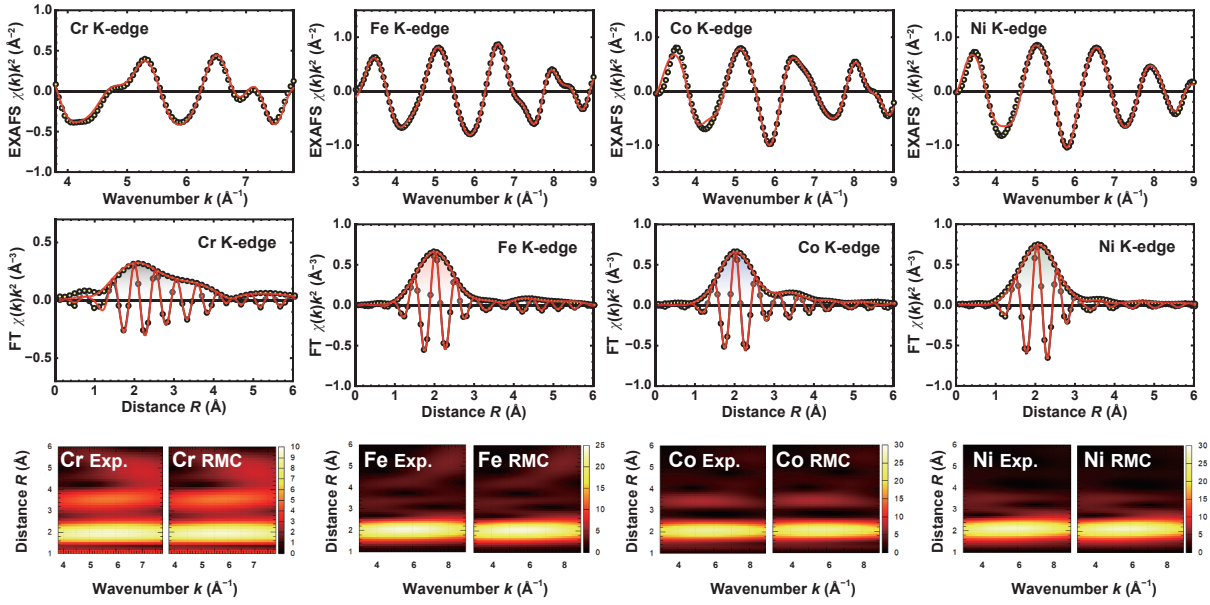

Figure 4 Experimental (symbols) and RMC-calculated (red lines) K-edge EXAFS spectra $\chi(k)k^2$ of Cr, Fe, Co, and Ni, as well as their Fourier and Morlet wavelet transforms for the $Cr_{20}Mn_{26}Fe_{18}Co_{19}Ni_{17}$ film at 300 K. Note that the peaks in the FTs are located at distances that are slightly shorter than their crystallographic values because the FTs were not corrected for the phase shift present in the EXAFS equation.

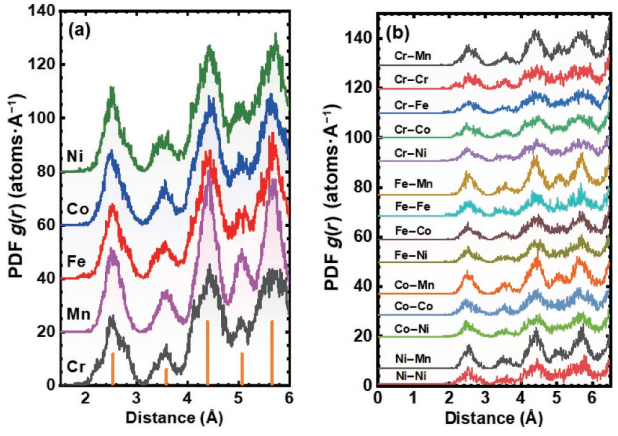

Figure 5 Pair distribution functions $g(r)$—(a) total and (b) partial—for the $Cr_{20}Mn_{26}Fe_{18}Co_{19}Ni_{17}$ film at 300 K extracted from K-edge EXAFS spectra of Cr, Fe, Co, and Ni using the RMC method (Mn K-edge EXAFS was not used in the simulations).

neighboring metal atoms for each principal component represent a self-consistent solution that is in good agreement with all available experimental EXAFS data in both k and R spaces describing the configuration-averaged local environment around a particular absorber.

The extracted total PDFs (Fig. 5(a)) are very similar to each other with only variations in their relative peak intensities and peak broadening. Interestingly, despite that the Mn K-edge was not fitted, the peaks in the total and partial PDFs of Mn are the narrowest ones: Usually, RMC analysis tends to broaden distributions that are not included in the fit. The narrow peaks of Mn PDFs denote that the positions of Mn atoms in the simulation box are well constrained by PDFs of the other constituents. Further comparison of the extracted PDFs with those of pure metal foils (see Ref. [51]) demonstrates that independently of the initial crystallographic ordering characteristic for pure metals (body-centered cubic (bcc) for Cr and Fe, hexagonal close packed (hcp) or fcc for Co and Ni, and α-phase with the space group $I\bar{4}3m$ (217) for Mn), the number of peaks and their positions within the first five coordination shells indicate a uniform short-range structure of the alloy with all atoms located in the fcc lattice without any signatures of additional crystallographic phases. Thus, all principal components of the Mn-rich CrMnFeCoNi film reproduce the fcc structure on the short-range atomic scale, confirming the previous results from Ref. [72], where TEM analysis demonstrated the existence of the nanocrystalline grain structure for the films prepared similarly and resolving ambiguity about nanocrystallinity or amorphous ordering of the entire film assumed from XRD.

The mean interatomic distances r and the mean square relative displacements σ^2 (see Table 1) were numerically obtained as the first and second moments of the total PDFs for atoms of each type. Besides, the MSDs were calculated directly from the final (relaxed) atomic coordinates of atoms in the simulation box relative to their ideal positions in the fcc lattice. Usually, MSDs are extracted from X-ray or neutron diffraction data and are not accessible from the EXAFS data analysis. The extracted mean distances r to the neighboring atoms are in the range of 2.54–2.55 Å for absorbers of each type without showing any visible preferences. These distances are noticeably larger as compared to the ones calculated for the hcp/fcc Co (2.51/2.52 Å) and fcc Ni foils (2.50 Å) [51]. As mentioned in Ref. [51], such an enlargement could be partially assigned to the atomic heterogeneity of the Cantor alloy where the larger sizes of Cr and Fe atoms force the atomic volume of the alloy to expand. Besides, the existing magnetic interactions can influence the final positions of all atoms, determining their lattice displacements. The MSRD σ^2 values related to Fe, Co, and Ni absorbers as extracted from the total PDFs are close to each other and are in the range of 0.040–0.043 Å^2; the σ^2 related to Cr is slightly larger (0.049 Å^2), while for Mn atoms this value is significantly smaller (0.028 Å^2). The same tendency was observed for the MSD values: Fe, Co, and Ni atoms have very closed MSDs in the range of 0.053–0.058 Å^2, and the Cr MSD is slightly larger and equal to 0.068 Å^2, whereas the MSD of Mn is much smaller and equal to 0.029 Å^2. This suggests the presence of a stronger disorder at Cr sites—There are larger uncertainties and variations in distances to the nearest-neighbors around Cr absorbers, and at the same time—the more ordered (more positionally defined) Mn sites. In general, the nanocrystalline Mn-rich CrMnFeCoNi film is more disordered in all shells at RT than the single-phase fcc-structured $Al_{0.3}CrFeCoNi$ [37] and the equiatomic bulk Cantor alloy [51] (as follows from PDFs), which agrees with the corresponding XRD patterns.

The MSD values of Cr, Fe, Co, and Ni in the studied thin film are about 3–4 times larger than in the pure bulk metals (the last column in Table 1) suggesting the presence of larger static disorder in the Mn-rich $Cr_{20}Mn_{26}Fe_{18}Co_{19}Ni_{17}$. On the contrary, the MSD value of Mn in the HEA film is smaller than that in the foil due to the presence of four crystallographically inequivalent Mn sites in an exotic crystal structure of α-Mn [73].

According to partial PDFs (Fig. 5(b)), the distribution of interatomic distances in the nearest-neighbor pairs of metal atoms is in the range of 2.53–2.56 Å (Table 2). The MSRDs σ^2 values for pairs of atoms including only Fe, Co, and Ni are close to each other and equal to 0.041–0.048 Å^2. The values for pairs including Cr atoms are larger (except Cr–Mn) and are in the range of 0.048–0.059 Å^2, the largest value was found for the Cr–Cr pair as 0.059 Å^2. The values for pairs including Mn atoms are smaller (0.021–0.030 Å^2) with the smallest value of 0.021 Å^2 found for Mn–Mn pairs.

Analysing either total or partial PDFs, it was found that Cr atoms have the largest σ^2 and MSD values among all constituents (see Tables 1 and 2, respectively), in agreement with Refs. [37, 42, 50, 51]. Moreover, the averaged local environment of Cr atoms in the studied film is fairly more disordered than that in the Al-deficient single-phase fcc $Al_{0.3}CrFeCoNi$ bulk piece [37] and in the flakes of equiatomic Cantor alloy [51]. The latter fact is most likely related to the film preparation method, while the enlarged structural relaxations of Cr as compared to other constituents seem to be typical for the family of Cantor alloys, and would be a subject of more detailed studies in the future.

3.2 Magnetometry studies

Conventional magnetometry studies revealed a complex character of the magnetic ordering inside of the Mn-rich Cantor alloy film and uncovered several co-existing magnetic phases within a certain temperature range. All obtained phases were assigned to the volume of the film and do not represent the effects at the surface (e.g., surface oxidation). The temperature dependencies of the magnetic moment were recorded at +50 mT during heating in the temperature range of 5–380 K after zero-field cooling (ZFC) and FC in fields of +50 mT, +2 T, and +5 T, as shown in Fig. 6(a). The curves demonstrate the presence of two pronounced magnetic transitions at ~ 50 and ~ 29 K and a dependency of the magnetic moment on the applied magnetic field in the case of field-assisted cooling. Clear distinctions between ZFC and FC curves were found up to temperatures above RT.

For the equiatomic Cantor alloy, the presence of two magnetic transitions at low temperatures was discussed in detail in Ref. [53]: The first one was found at 93 K and was assigned to the transition from the paramagnetic (PM) to the spin-glass state, whereas the

Table 1 Structural parameters (r, MSRD, and MSD) extracted from the total PDFs of the $Cr_{20}Mn_{26}Fe_{18}Co_{19}Ni_{17}$ film. The MSD values extracted from PDFs of Cr, Mn, Fe, Co, and Ni pure metals are given for comparison[a]

	Phase in pure metal	r (Å) (±0.02 Å)	MSRD σ^2 (Å^2) (±0.003 Å^2)	MSD σ^2 (Å^2) (±0.003 Å^2)	MSD σ^2 (Å^2) (±0.003 Å^2) for pure metals
Cr	bcc	2.55	0.049	0.068	0.017 [51]
Mn	α-Mn	2.54	0.028	0.029	0.048
Fe	bcc	2.55	0.043	0.058	0.014 [51]
Co	hcp/fcc	2.55	0.040	0.053	0.017/0.023 [51]
Ni	fcc	2.55	0.040	0.053	0.017 [51]

[a]All average distances are about 2.54–2.55 Å; Cr (Mn) atoms have the largest (smallest) values of MSRD and MSD.

Table 2 Structural parameters (r and MSRD) extracted from the partial PDFs of the $Cr_{20}Mn_{26}Fe_{18}Co_{19}Ni_{17}$ film[a]

	r (Å)/MSRD σ^2 (Å^2)				
	Cr	Mn	Fe	Co	Ni
Cr	2.56/0.059	2.56/0.036	2.54/0.056	2.56/0.048	2.55/0.049
Mn	—	2.54/0.021	2.56/0.030	2.53/0.028	2.54/0.029
Fe	—	—	2.55/0.048	2.55/0.041	2.55/0.043
Co	—	—	—	2.54/0.043	2.55/0.041
Ni	—	—	—	—	2.55/0.044

[a]All average distances are about 2.53–2.56 Å; Cr atoms have the largest MSRD (except for Cr–Mn), and Mn atoms have the smallest MSRD.

second transition at 38 K is of ferromagnetic (FM) origin. In the case of the Mn-rich Cantor alloy film studied here, both transitions were found at lower temperatures, and the difference between ZFC and FC curves found at temperatures higher than 50 K points to a co-existence of the FM and PM phases up to 380 K. In the range 29–50 K the FM and spin-glass-like phases are assumed, while significant differences between these curves below 29 K suggest a redistribution of the FM and spin glass-like contributions. Thus, the observed magnetic transitions can be associated with the magnetic phase transformations of only a fraction of the film. Moreover, the FC curves recorded after the field-assisted cooling in +2 and +5 T are very similar (see Fig. 6(a)) and show the only difference in the value of the magnetic moments detected at 5 K. This difference corresponds to the coexistence of several magnetic phases. Full reversibility of FC temperature dependencies collected after ±5 T field-assisted cooling (see Fig. S1 in the Electronic Supplementary Material (ESM)) points out a full magnetic saturation of all non-collinear or magnetically frustrated regions inside the nanocrystalline film at magnetic fields of ±5 T.

The field-dependences of the magnetization recorded in the ±5 T field range at different temperatures after ZFC are shown in Fig. 6(b). All curves demonstrate a presence of FM and PM/spin glass-like contributions, and at temperatures higher than RT the diamagnetic input from a sample-holder is visible. The opening of the hysteresis curves is temperature-dependent (see inset in Fig. 6(b)) confirming the changes in the magnetic order with temperature. The largest values of the coercivity and the remnant magnetization are ~ 0.18 T and ~ 4.44 emu·g^{-1} at 5 K, respectively. These values drop sharply with rising a temperature up to 35 K. Besides, a very small exchange bias-like effect ($\Delta H_c^{(1)}$ = −83 Oe) was observed only at 5 K, whereas at higher temperatures ΔH_c was smaller than the remnant fields of the MPMS system (up to ±33 Oe). However, the pronounced kinks in the zero-field region were noticed for the field dependences collected up to 35 K.

The complexity of magnetic ordering in the Mn-rich Cantor alloy film can be additionally illustrated by the field dependence of the magnetic moment recorded within a smaller field range of ±2 T right after the field-assisted cooling in ±2 T. The resulting field dependencies are shown in Fig. 6(c). The hysteresis loops were found to be shifted in the magnetization direction (vertical shift) up to ~ 2.02 emu·g^{-1}, and at the same time a horizontal shift in the magnetic field direction up to ±0.125 T is visible. The direction of these vertical and horizontal shifts is governed by the direction of the applied magnetic field during field-assisted cooling. The observed vertical shift is much smaller than the ones reported in Ref. [53] for the bulk slab of equiatomic Cantor alloy, and the magnetic behavior of the studied Mn-rich nanocrystalline film is different compared to the macroscopic flakes of the single-phase equiatomic fcc CrMnFeCoNi [51] as well. The presence of the sizable horizontal shift (exchange bias) assumes that there are magnetic contributions that are antiferromagnetically coupled with the external field. Accordingly, the ferromagnetically coupled moments can be pinned by the antiferromagnetically coupled ones, causing a small excess moment manifested as the vertical shift of the hysteresis loop.

The behavior of hysteresis loops observed after the field-assisted cooling in ±2 T can be assigned to the presence of disordered regions where a strong competition between ferromagnetic and antiferromagnetic couplings of the nearest-neighbors is anticipated. In these regions, the existence of frustrated magnetic moments is highly possible leading to frozen magnetic contributions enforced by the direction of FC. Since all individual PDFs of principal components (except Mn) demonstrate rather large structural displacements (Table 2), all constituents can actively participate in the formation of such competing couplings.

Calculations show evidence that the distribution of ferromagnetic and antiferromagnetic interactions in the Cantor alloy is very sensitive to the size of the fcc unit cell as well as to the local configurations of the nearest-neighbors [33, 40, 53]. Moreover, the antiferromagnetic alignment of Cr with respect to ferromagnetically coupled Fe, Co, and Ni is energetically favourable [40], and, in general, Cr atoms prefer to align antiferromagnetically to the cumulative magnetic moment of their first coordination shell regardless of the initial local arrangements [53]. The same tendency in the magnetic moment alignment was theoretically predicted for the four-component fcc alloy CrFeCoNi [74] and found experimentally in the sub-surface volume of $Al_{0.3}$CrFeCoNi HEA [37] and equiatomic CrMnFeCoNi [33].

[(1)] ΔH_c can be expressed through coercivities found for the field sweeps down and up (H_{c-} and H_{c+}, respectively) as $\Delta H_c = 0.5 \cdot (H_{c-} + H_{c+})$.

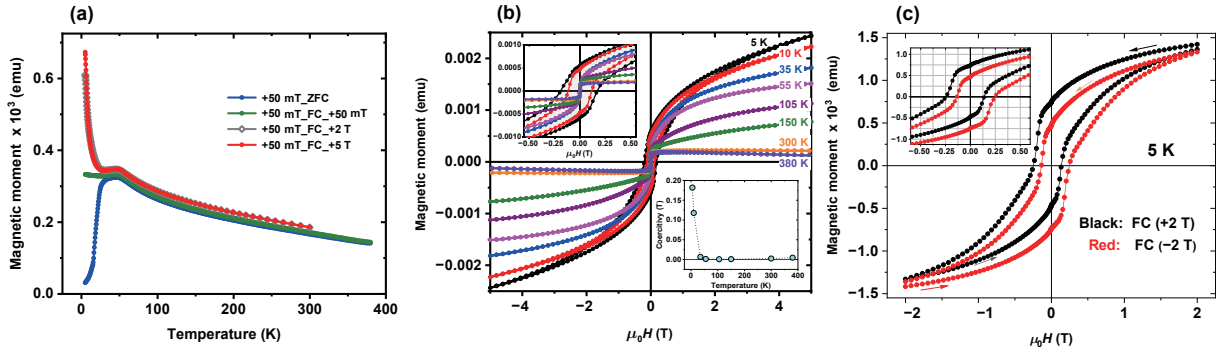

Figure 6 Magnetic behavior of the $Cr_{20}Mn_{26}Fe_{18}Co_{19}Ni_{17}$ film according to conventional magnetometry. (a) Temperature dependence of magnetization recorded at +50 mT after ZFC and FC under +50 mT, +2 T, and +5 T applied magnetic fields. (b) Magnetic hysteresis curves recorded at different temperatures after ZFC (the insets show the enlarged region near zero field and the temperature dependence of coercivity). (c) Magnetic hysteresis curves recorded in the field range of ±2 T after field-assisted cooling in ±2 T, respectively.

The alignment and value of Mn magnetic moment can vary significantly depending on the unit cell volume of the Cantor alloy [40] and can favour the ferrimagnetic alignment in the film [75]. Thus, for the nanocrystalline HEA film, a very complex magnetic ordering due to the high sensitivity of the individual magnetic moments to the local environment and a large amount of nanocrystallite grain boundaries, which formed during the film growth, was anticipated. Besides, magnetically frustrated or non-collinear magnetic regions are expected to be distributed along the whole volume of the film due to the high heterogeneity of the Cantor alloy (caused by five principal elements) at the atomic scale. The pinning of the magnetic moments on the grain boundaries and other lattice defects during the field sweep is thus not surprising and supports the presence of antiferromagnetically coupled moments in the volume of the film. These factors can also explain the variations in magnetic properties of HEAs composed of the same principal components taken in different compositions or prepared according to different routes.

The experimental evaluation of the relative magnetic coupling of each constituent in the studied film could be carried out by the synchrotron-based element-specific XMCD technique; the results obtained with soft X-rays are presented in Section 3.3.

3.3 XANES and XMCD studies with soft X-rays

3.3.1 Surface oxidation of the Cantor alloy film

XANES spectra recorded at the $L_{2,3}$ absorption edges of all 3d constituents as well as at the oxygen K absorption edge are shown in Figs. 7 and 8(a). The spectra were used to check the oxidation states of 3d ions in the sub-surface volume (down to several nm) of the $Cr_{20}Mn_{26}Fe_{18}Co_{19}Ni_{17}$ film. Fe and Co oxidation in the naturally formed top oxide layer was found to be stronger as compared to those reported previously for the fcc $Al_{0.3}CrFeCoNi$ HEA using XANES [37] and the four-component fcc-structured medium entropy alloy CrFeCoNi using XPS [76, 77], while Cr and Ni have the oxidation degrees characteristic for these systems.

The evaluation of Cr XANES spectra shows that Cr forms Cr_2O_3 oxide (with Cr^{3+}). Mn is assumed to be oxidized to Mn^{2+} since the lineshape of the Mn XANES spectrum is in-between the

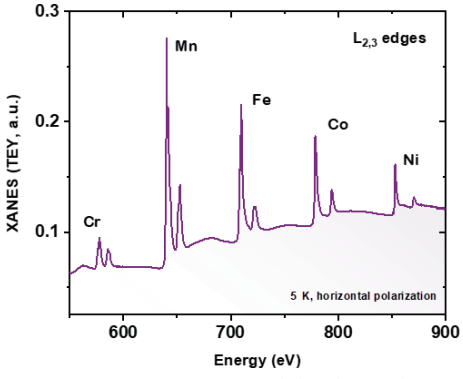

Figure 7 Overview XANES spectrum recorded at the $L_{2,3}$ absorption edges of Cr, Mn, Fe, Co, and Ni at 5 K with horizontally polarized X-rays from the naturally oxidized $Cr_{20}Mn_{26}Fe_{18}Co_{19}Ni_{17}$ film. A larger amount of Mn atoms in the probed sub-surface volume of the film is apparent.

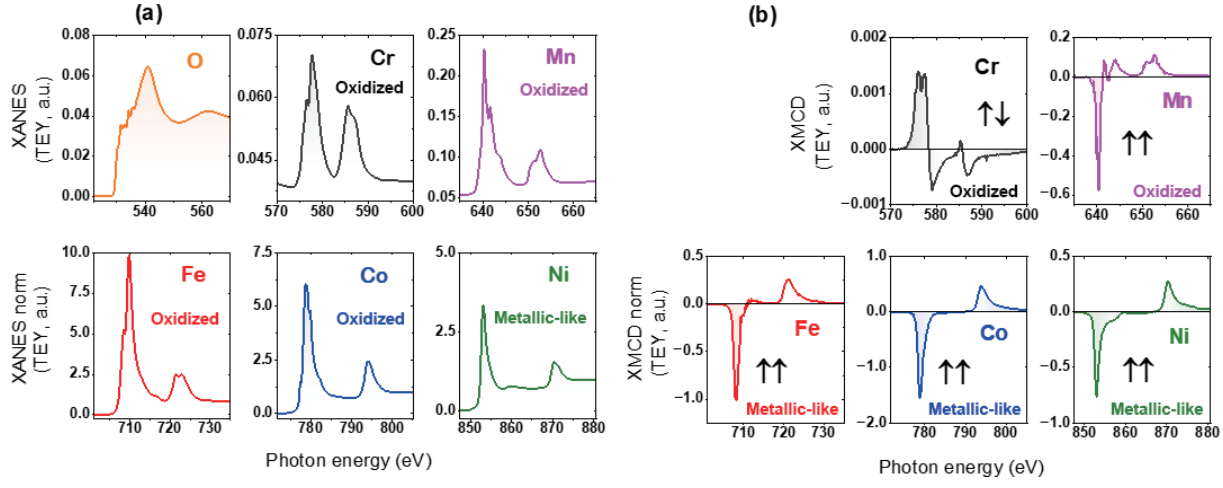

Figure 8 (a) XANES and (b) XMCD spectra recorded at the $L_{2,3}$ absorption edges of Cr, Mn, Fe, Co, and Ni at 5 K with circularly polarized X-rays from the oxidized $Cr_{20}Mn_{26}Fe_{18}Co_{19}Ni_{17}$ film under +4 T magnetic field. The XANES at the oxygen K absorption edge is shown for completeness. The sign of the XMCD signals points out the alignment of the 3d constituent magnetic moments as schematically depicted on each plot. The largest contribution to the TEY signal (up to 80%) for these energy ranges is coming from the top 1–2 nm of the film; the rest of the signal is coming from the depths up to 6–9 nm.

MnO/MnS references [78, 79]. Fe and Co atoms are known for their ability to form different oxides at the surface of HEAs, and here the presence of Fe^{3+}-like and Co^{2+}-like oxidation states was revealed. As expected, Ni atoms were found to retain a metallic-like state. The tendency towards strong oxidation of Cr, Mn, Fe, and Co, while keeping the metal-like nature of Ni, is typical for Cantor alloy and was found at several points along the sample surface. Meanwhile, the lineshape of oxygen XANES spectra varied significantly at each probing point.

The corresponding XMCD spectra for all principal components of the alloy are shown in Fig. 8(b): The lineshape of the XMCD spectra points out the strongly oxidized magnetic Cr and Mn, while the pronounced XMCD signal for Fe, Co, and Ni can be described as metallic-like. Since Cr_2O_3 is an antiferromagnet, the net magnetic moment of Cr atoms from the top oxide layer is expected to be negligible. So, the observed XMCD signal at the Cr $L_{2,3}$ absorption edges could have several reasons, among which are: canted Cr moments in Cr_2O_3 due to different types of distortions in the top oxide layer, a specific distribution of all principal elements within the top oxide layer leading to non-vanishing Cr magnetic moments at the interface between the film and the Cr-rich top oxide, or Cr magnetic moments from the alloy under the oxide contributing to the collected signal. Similarly, the XMCD signal of Mn can be described as a superposition of signals from partially oxidized and metallic-like atoms in the top layer or the alloy underneath (to separate the overlapping contributions in the XMCD signals might be possible in some cases by the element-specific hysteresis curves). Contrary to this, the magnetic contributions associated with Fe and Co oxides are negligible as compared to the signal from the metallic-like atoms. Thus, due to the FM response of Fe and Co demonstrated in Fig. 8(b), we suppose that there is a fraction of Fe and Co atoms from the alloy under the top oxide in the sub-surface volume of the film probed with soft X-rays. The same is valid for Mn and Ni atoms as well. So, some quantitative estimations about the thickness of the top oxide layer (several nm) can be done due to the certain limitations for the probing depths accessible by the XANES/XMCD techniques with soft X-rays.

Previously, a Cantor alloy film prepared in the same way was studied by APT in Ref. [72] after annealing in a vacuum. The surface oxidation was found to be within about 3 nm depth below the top surface as it was quantitatively confirmed by the concentration profile enriched with oxygen. Cr oxide formed at the top of the film extends from the top of the sample into its interior along grain boundaries.

Due to oxidation, it is barely possible to calculate correctly the amount of each type of atoms and ions in the probing volume and to make conclusions about the sub-surface composition of the nanocrystalline film and its possible change as compared to the volume. Moreover, a number of 3d holes needed for a proper evaluation of 3d magnetic moments based on the optical sum rules analysis of the XMCD spectra [80, 81] could not be done even with a rough accuracy. However, considering the sign of the XMCD signal it is still possible to establish the alignment of the 3d magnetic moments for each probed constituent with respect to the magnetic field. The schematic coupling of these moments is depicted for each principal component in Fig. 8(b): According to the XMCD studies using soft X-rays, the total net magnetic moment of Cr aligns antiparallel to the external magnetic field while Mn, Fe, Co, and Ni net magnetic moments align parallel to it. The same alignments were previously established for the oxide-free surface of an equiatomic CrMnFeCoNi single crystal in Ref. [33] by XMCD with soft X-rays, despite the calculations [40] predicting the antiparallel alignment of Mn magnetic moment in the fcc Cantor alloy of the same unit cell. Other works [33, 53, 75, 82] report a much more complicated magnetic ordering of Mn that results in a very small Mn net magnetic moment and its parallel alignment to the magnetic field.

Another advantage of XMCD is the possibility to collect element-specific hysteresis loops to disentangle the magnetic contributions of each constituent element of a multicomponent system to the total magnetic field dependence recorded by conventional SQUID/VSM magnetometry. Examples of such hysteresis loops for the Mn-rich CrMnFeCoNi film with a natively oxidized surface are presented in Fig. 9. The magnetic behavior of Cr and Mn is principally different from that of Fe, Co, and Ni. XMCD asymmetry was calculated as $(TEY(\sigma^+) - TEY(\sigma^-))/(TEY(\sigma^+) + TEY(\sigma^-))$, where $\sigma^{+,-}$ are incoming circular polarizations of X-ray photons with opposite (right and left) helicities and with energies corresponding to the maximum of the XMCD signal presented in Fig. 8(b). The open hysteresis loops with similar shapes and with ~ 0.055 T coercivity were found for Fe, Co, and Ni constituents. On the other hand, the element-specific hysteresis of Cr exhibits antiferromagnetic coupling with the external magnetic field and opening with very close values of coercivities. Interestingly, XMCD asymmetry of Cr shows a faster magnetic saturation as compared with Fe, Co, and Ni. Finally, the field-dependence of Mn XMCD asymmetry reveals a superposition of the open hysteresis and the linear dependence in agreement with the assumption of the presence of metallic-like and oxidized Mn contributions in the Mn XMCD signal. The sign of the Mn XMCD asymmetry confirms the ferromagnetic coupling of Mn net magnetic moment to the external magnetic field. The similarity in the coercivities found for each principal component can be used as proof that ferromagnetic/antiferromagnetic contributions can be assigned to atoms in the alloy under the top oxide and thus the sign of the individual principal components of the alloy is correctly established. The small discrepancy in coercivities found for the surface atoms, as compared to the hysteresis loop observed by conventional magnetometry, we mostly relate to the presence of surface effects.

3.3.2 Predominantly oxide-free Cantor alloy film after in situ cleaning

To probe the magnetic properties from the oxide-free surface of the Cantor alloy, the film was cleaned *in situ* by Ar^+ sputtering just before collecting X-ray absorption spectra. XANES and XMCD spectra recorded at the $L_{2,3}$ absorption edges of all 3d constituents at 10 K are shown in Fig. 10. The spectra reveal the metallic states

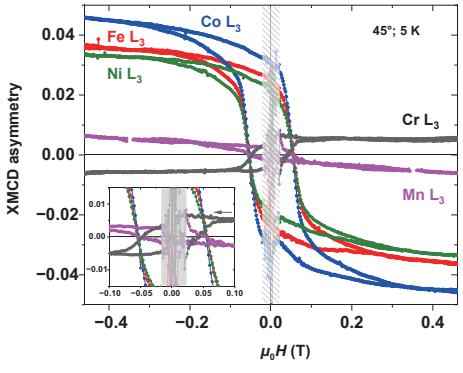

Figure 9 Element-specific hysteresis curves recorded at the maximum of the XMCD signals observed at the $L_{2,3}$ absorption edges of Cr (576.2 eV), Mn (640.3 eV), Fe (708.14 eV), Co (778.87 eV), and Ni (852.75 eV) from the oxidized $Cr_{20}Mn_{26}Fe_{18}Co_{19}Ni_{17}$ film. XMCD asymmetry was calculated as $(TEY(\sigma^+) - TEY(\sigma^-))/(TEY(\sigma^+) + TEY(\sigma^-))$, where $\sigma^{+,-}$ are incoming circular polarizations of X-rays with opposite helicities. The TEY signal instability region at small magnetic fields is shown by the patterned area.

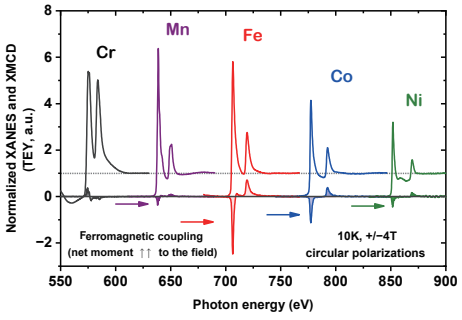

Figure 10 XANES and XMCD spectra recorded at the $L_{2,3}$ absorption edges of Cr, Mn, Fe, Co, and Ni from the *in situ* cleaned $Cr_{20}Mn_{26}Fe_{18}Co_{19}Ni_{17}$ film (Ar^+, 45°, 1 keV, 1 h 20 min) while the sample is in magnetic saturation at ±4 T. The measurements were performed at 10 K with circularly polarized X-rays.

of Fe, Co, and Ni constituents without any detectable level of surface oxides, while Cr and Mn XANES spectra indicate slight oxidation recognizable by splitting of the corresponding $L_{2,3}$-edge white lines (see Fig. S2 in the ESM). The reason for the observed remaining oxidation can be related to the presence of the residual oxygen in the UHV chamber: Cr and Mn are known for their reactive ability to form Cr_2O_3 and MnO oxides whereas oxidation of Fe, Co, and Ni down to FeO, CoO, and NiO (as well as to Fe_3O_4 and Fe_2O_3), respectively, is much slower. The performed surface treatment is not as mild as cleaning by Ar^+ plasma [33] and can lead to changes in the film composition in the sub-surface volume of the film, as evidenced by changes in the relative edge jumps of XANES (see Fig. S3 in the ESM). Thus, such a treatment could be considered as only the first step towards the preparation of the thermodynamically stable oxide-free surface of the Cantor alloy. The complete removal of Cr and Mn surface oxides is not a trivial task and should be realized in further works.

The sign of the XMCD signals observed at the Cr, Mn, Fe, Co, and Ni $L_{2,3}$ absorption edges confirms the earlier conclusions about the antiparallel coupling of Cr magnetic moment to the external magnetic field while all other principal components are coupled parallel to it. This also agrees with the experimental results previously demonstrated in Ref. [33]. It is worth noting that soft X-rays XANES and XMCD are surface-sensitive techniques and cannot be used to ambiguously prove the volume magnetic moments of constituents in the case of their complex magnetic order (as shown by calculations for Mn atoms in Cantor alloys [33, 53, 82]). Yet, they still can be used for uncovering the presence of characteristic changes in the electronic structure of constituents due to atomic heterogeneity of HEAs and for quantitative estimations of the spin and orbital contributions to the magnetic moment of principal components at the surface.

The normalized XANES and XMCD spectra presented in Fig. 10 for Fe, Co, and Ni reveal the variations in white line intensities related to $2p_{1/2,3/2} \rightarrow 3d$ transitions in the HEA film and the visible changes in the dichroic magnetic signals of principal components as compared with reference 3d metals (see Fig. S4 in the ESM). The integrals over the white lines (without the so-called step-function) can be used to estimate the number of 3d holes ($n_{\_3d\_holes}$) [80, 81] for the corresponding elements at the surface of the Cantor alloy. Accordingly, considering the experimentally observed spectra weighted by the spectra of the reference films and the theoretically calculated $n_{\_3d\_holes}$ values from Ref. [83], the estimations of $n_{\_3d\_holes}$ for the present case were done. An increase in the number of Fe 3d holes was found as compared to pure Fe metal while a decrease in the number of 3d holes was observed for Co and Ni. The XMCD signal at the Fe $L_{2,3}$ absorption edges is only slightly smaller at the surface of the HEA as compared to the pure metal film while the XMCD signal at the Co and Ni $L_{2,3}$ absorption edges is sizably smaller as compared to the references.

The results of further calculations of the net magnetic moments at the surface of the HEA in absolute μ_{Bohr} units [80, 81], the experimental $n_{\_3d\_holes}$ values, orbital-to-spin ratio, and their comparisons with those values for bulk Fe, Co, and Ni are presented in Table 3. The total magnetic moment of Fe (~ 2.47 μ_{Bohr}) is within an error bar of its bulk value (2.22 μ_{Bohr}), while the magnetic moments of Co (~ 1.12 μ_{Bohr}) and Ni (~ 0.42 μ_{Bohr}) are smaller as compared with the reference bulk metals. The estimations of Cr and Mn magnetic moments were skipped due to a large systematic uncertainty related to the small spin-orbit splitting of Cr and Mn $2p_{3/2}$ and $2p_{1/2}$ core levels, which results in their very close $L_{2,3}$ absorption edges and the significant overlap of the corresponding white lines. The presence of remaining partial oxidation additionally increases the uncertainty in the values of magnetic moments. The magnetic dipole term $\langle T_z \rangle$ involved in the calculation of the spin magnetic moment [80, 81] and associated with the intra-atomic spin asphericity could not be quantitatively estimated in general. For bulk systems with cubic symmetry, it is negligible, while for surfaces and low dimensional systems it can bring up to 20% uncertainty of the spin moment. Therefore, assuming the cubic symmetry of atoms at the surface of the alloy and taking into account a rather small spin-orbit coupling of 3d elements, the $\langle T_z \rangle$ term was neglected during the calculations of Fe, Co, and Ni spin magnetic moments (as it was previously done in Refs. [33, 37]). The element-specific hysteresis loops from the *in situ* cleaned surface are shown in Fig. 11, demonstrating magnetic saturation at fields below 1 T, and confirming the antiparallel coupling of Cr atoms.

The obtained values of effective spin magnetic moments at the surface of the HEA were compared with those of isolated atoms (pure d-electron magnetism) and in the bulk metals in Fig. 12. The effective spin magnetic moments for Co and Ni are smaller than the corresponding bulk values, regardless of the symmetry breaking at surfaces that leads to the increased values of spin and orbital contributions in general, and any breaking of cubic symmetry results in the additionally increased $\langle T_z \rangle$ contribution to the effective spin moment. The same tendency was previously noticed in Refs. [33, 37] although the values of the obtained moments are different. The effective spin magnetic moment of Fe atoms is closer to the theoretical value from Ref. [33] (2.12 μ_{Bohr})

Table 3 The estimated values of the number of 3d holes ($n_{\_3d\_holes} = 10 - n_{\_3d\_electrons}$), the orbital, spin, and total magnetic moments in μ_{Bohr}, and orbital-to-spin ratio for Fe, Co, and Ni constituents at the surface of the *in situ* cleaned Cantor alloy film together with reference numbers for the corresponded bulk metals. The values of the orbital magnetic moments are the estimations of their order of magnitudes only

	Number of 3d holes at the surface of HEA	Orbital magnetic moment at the surface of HEA (μ_{Bohr})	Spin magnetic moment at the surface of HEA (μ_{Bohr})	Orbital-to-spin ratio at the surface of HEA	Total magnetic moment at the surface of HEA (μ_{Bohr})	Number of 3d holes for bulk metal	Orbital-to-spin ratio for bulk metal	Magnetic moments for bulk metal (μ_{Bohr})
Fe	4.31	0.06	2.41	0.025 (fcc)	2.47 ± 0.50	3.4	0.042 (bcc)	2.22
Co	2.37	0.13	0.99	0.131 (fcc)	1.12 ± 0.22	2.5	0.099 (hcp)	1.72
Ni	1.10	0.05	0.37	0.135 (fcc)	0.42 ± 0.08	1.5	0.100 (fcc)	0.62

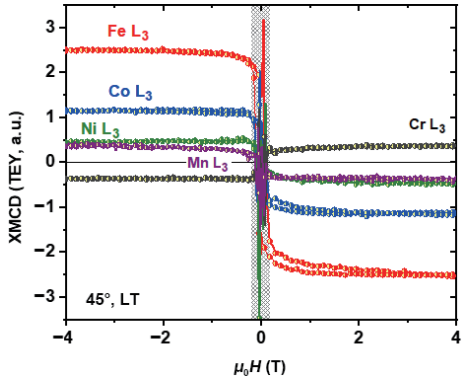

Figure 11 Element-specific hysteresis curves recorded at the maximum of the XMCD signals observed at the $L_{2,3}$ absorption edges of Cr (574.5 eV), Mn (638.0 eV), Fe (706.4 eV), Co (777.4 eV), and Ni (851.7 eV) from the *in situ* cleaned $Cr_{20}Mn_{26}Fe_{18}Co_{19}Ni_{17}$ film. The TEY signal instability region at small magnetic fields is shown by the patterned area.

provided for the equiatomic CrMnFeCoNi alloy by Korringa–Kohn–Rostoker (KKR) calculations employing the coherent potential approximation (CPA) than it was found experimentally in the same work. Importantly, these types of calculations can effectively treat the compositional disorder of the multicomponent system. The expected values of effective spin moments for Cr and Mn are marked by the patterned areas in Fig. 12: Cr demonstrates antiparallel coupling to the other elements in agreement with first-principles calculations for several medium- and high-entropy alloys [53, 82, 84], while the most intriguing discrepancy with theory calculations including the value and the opposite sign of the magnetic moment coupling was found for Mn atoms.

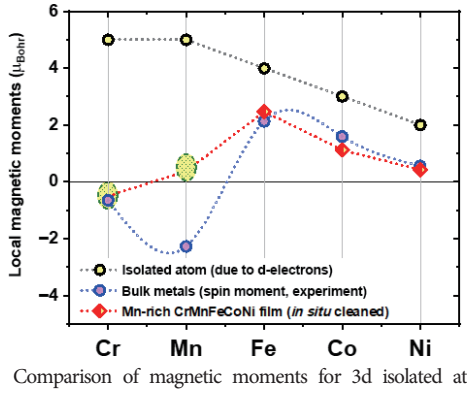

Figure 12 Comparison of magnetic moments for 3d isolated atoms, bulk metals, and elements at the surface of the *in situ* cleaned $Cr_{20}Mn_{26}Fe_{18}Co_{19}Ni_{17}$ film. The values for Cr and Mn magnetic moments are expected to be within the patterned areas.

4 Conclusions

The detailed element-specific studies of novel multifunctional materials can lift the veil from the behavior of their individual components at the atomic scale, which can in turn explain the differences in macroscopic properties of systems that comprise similar constituent elements. In this study, we employed hard and soft X-ray absorption spectroscopy to perform structural and magnetic characterization of the $Cr_{20}Mn_{26}Fe_{18}Co_{19}Ni_{17}$ HEA film at the K and $L_{2,3}$ absorption edges of principal components. This made it possible to complement macroscopic characterization done by XRD and conventional magnetometry, and to clarify the details of the local crystallographic environment of atoms and their magnetic couplings.

The peculiarities of the metal atom local structure in the film have been probed by EXAFS in combination with reverse Monte Carlo simulations, which allowed us to simultaneously fit the X-ray absorption spectra independently collected at four individual absorption edges within the same self-consistent structural model in the most unbiased manner. The resulting total and partial pair distribution functions of each principal component of the alloy point out a short-range fcc crystallographic surrounding around the absorbers of each type with very similar interatomic distances to their nearest-neighbors. Moreover, no crystallographic secondary phases were detected at the local scale. This information was hidden in the non-resonant XRD pattern due to their strong broadening caused by the size of nanocrystallites formed during the film growth. The displacements of atoms from the ideal lattice site positions are the largest for Cr, whereas Mn species demonstrate the smallest structural disorder. The rest components (Fe, Co, and Ni) exhibit intermediate values of displacements which are very similar to each other. These outcomes are consistent with the results available in the literature for other Cantor alloys, while the reason for such a behavior of Cr should be further clarified with the help of extensive first-principles calculations.

The oxidation states and magnetic properties of sub-surface atoms in the presence of natural oxide as a top layer have been probed by XANES and XMCD to clarify the significance of possible net magnetic moments carried by the oxidized atoms. Both of these quantities may affect the corrosion resistance and have an impact on the catalytic activity of HEAs. The oxidation states probed by XANES reveal the anticipated common trend with the strongest oxidation found for Cr and the almost metallic-like state for Ni; however, the magnetic behavior of sub-surface atoms was surprising. The shape of the XMCD signal found for Fe, Co and Ni suggests that the oxidized atoms do not bear sizeable net magnetic moments as compared to the magnetic moments associated with metallic atoms from the alloy underneath. Meanwhile, oxidized Cr^{3+} and Mn^{2+} demonstrate small magnetic signals, the sign of which indicates antiparallel and parallel coupling with the external magnetic field, respectively. Element-specific hysteresis loops recorded at energies corresponding to the maximum of the observed XMCD signals for these components are very different: Cr exhibits the field dependence which is similar to Fe, Co, and Ni constituents, and only the sign and the amplitude of the XMCD signal vary, while Mn shows a well pronounced linear field-dependence in addition to a small opening of the hysteresis. A reason for such differences has to be clarified further, and, most probably, it relates to a different ratio of magnetic contributions from oxidized and metallic Cr and Mn atoms at the chosen energies, respectively. The sign of the XMCD signal found for all constituent elements is consistent with results presented in the literature for another XMCD experiment performed with the equiatomic Cantor alloy but contradicts the results of density functional theory (DFT) calculations. The conventional magnetometry is not sensitive to such information, and it was applied to reveal the opening of the hysteresis at low temperatures of 5–35 K, the presence of co-existing magnetic phases up to room temperature, and slightly shifted temperatures of several phase transitions as compared with the equiatomic Cantor alloy.

The *in situ* cleaning of the film resulting in a predominantly oxide-free surface of high-entropy alloy provides a possibility to evaluate quantitatively the magnetic moments of Fe, Co, and Ni constituents at the surface of HEA film and to compare them further with known magnetic moments of the reference metals. The differences found suggest a strong dependence of magnetic moments on surface treatment as expected, and visible changes are present in the electronic structures of these elements.

In general, our work demonstrates the results of advanced

characterization of the Mn-rich high-entropy Cantor alloy film at the atomic and macroscopic scales and underlines the similarities and differences in structural and magnetic properties as compared to other high-entropy systems. Considered altogether, some common trends, e.g., in the component-dependent lattice distortions can be revealed despite a very diverse macroscopic behavior. Further efforts to achieve a fully oxide-free and thermodynamically stable high-quality surface and its detailed characterization by XANES/XMCD with soft and hard X-rays will make it possible to understand the impact of high-entropy effects at the surface of different HEAs as compared to their entire volume. Such knowledge can be further exploited to design materials with improved surface performance and to allow their scaling down to low dimensions required for the continuously developing vital technologies.

Acknowledgements

The authors thank the Helmholtz-Zentrum Berlin for the provision of access to synchrotron radiation facilities and allocation of synchrotron radiation at the BAMline, UE46_PGM-1, and VEKMAG beamlines of BESSY II at HZB. The measurement time for magnetometry studies at the HZB CoreLab for Quantum Materials is acknowledged as well. The financial support for the VEKMAG project and the PM2-VEKMAG beamline by the German Federal Ministry for Education and Research (BMBF # 05K10PC2, # 05K10WR1, # 05K10KE1, and # 05K19KEA) and by HZB is cordially acknowledged by all co-authors. Steffen Rudorff is acknowledged for technical support. A. Sm. also acknowledges personal funding from CALIPSOplus project (the Grant Agreement No. 730872 from the EU Framework Programme for Research and Innovation HORIZON 2020). Institute of Solid State Physics, University of Latvia as the Center of Excellence has received funding from the European Union's Horizon 2020 Framework Programme H2020-WIDESPREAD-01-2016-2017-TeamingPhase2 under grant agreement No. 739508, project CAMART2. B. X., A. S. and A. L. thank the DFG for financial support within the projects DE 796/11–1 and LU1175/22–1.

Funding note: Open Access funding enabled and organized by Projekt DEAL.

Electronic Supplementary Material: Supplementary material (reversibility of the temperature dependence of magnetization recorded after the field-assisted cooling in the opposite fields, splitting of the XANES white lines recorded at the $L_{2,3}$ absorption edges of Cr and Mn, illustration of a stoichiometry change in the sub-surface probing volume, and comparison of XANES/XMCD spectra for the surface Fe, Co and Ni atoms of the HEA and reference films) is available in the online version of this article at https://doi.org/10.1007/s12274-022-5135-3.

References

[1] Cantor, B.; Chang, I. T. H.; Knight, P.; Vincent, A. J. B. Microstructural development in equiatomic multicomponent alloys. *Mater. Sci. Eng.* **2004**, *375–377*, 213–218.

[2] Yeh, J. W.; Chen, S. K.; Lin, S. J.; Gan, J. Y.; Chin, T. S.; Shun, T. T.; Tsau, C. H.; Chang, S. Y. Nanostructured high-entropy alloys with multiple principal elements: Novel alloy design concepts and outcomes. *Adv. Eng. Mater.* **2004**, *6*, 299–303.

[3] Miracle, D. B.; Senkov, O. N. A critical review of high entropy alloys and related concepts. *Acta Mater.* **2017**, *122*, 448–511.

[4] Sarkar, A.; Wang, Q. S.; Schiele, A.; Chellali, M. R.; Bhattacharya, S. S.; Wang, D.; Brezesinski, T.; Hahn, H.; Velasco, L.; Breitung, B. High-entropy oxides: Fundamental aspects and electrochemical properties. *Adv. Mater.* **2019**, *31*, 1806236.

[5] Albedwawi, S. H.; AlJaberi, A.; Haidemenopoulos, G. N.; Polychronopoulou, K. High entropy oxides-exploring a paradigm of promising catalysts: A review. *Mater. Des.* **2021**, *202*, 109534.

[6] Ma, Y. J.; Ma, Y.; Wang, Q. S.; Schweidler, S.; Botros, M.; Fu, T. T.; Hahn, H.; Brezesinski, T.; Breitung, B. High-entropy energy materials: Challenges and new opportunities. *Energy Environ. Sci.* **2021**, *14*, 2883–2905.

[7] Tsai, K. Y.; Tsai, M. H.; Yeh, J. W. Sluggish diffusion in Co-Cr-Fe-Mn-Ni high-entropy alloys. *Acta Mater.* **2013**, *61*, 4887–4897.

[8] Kao, Y. F.; Chen, S. K.; Sheu, J. H.; Lin, J. T.; Lin, W. E.; Yeh, J. W.; Lin, S. J.; Liou, T. H.; Wang, C. W. Hydrogen storage properties of multi-principal-component $CoFeMnTi_xV_yZr_z$ alloys. *Int. J. Hydrogen Energy* **2010**, *35*, 9046–9059.

[9] Sahlberg, M.; Karlsson, D.; Zlotea, C.; Jansson, U. Superior hydrogen storage in high entropy alloys. *Sci. Rep.* **2016**, *6*, 36770.

[10] Pedersen, J. K.; Batchelor, T. A. A.; Bagger, A.; Rossmeisl, J. High-entropy alloys as catalysts for the CO_2 and CO reduction reactions. *ACS Catal.* **2020**, *10*, 2169–2176.

[11] Löffler, T.; Savan, A.; Meyer, H.; Meischein, M.; Strotkötter, V.; Ludwig, A.; Schuhmann, W. Design of complex solid-solution electrocatalysts by correlating configuration, adsorption energy distribution patterns, and activity curves. *Angew. Chem., Int. Ed.* **2020**, *59*, 5844–5850.

[12] Yao, Y. G.; Huang, Z. N.; Li, T. Y.; Wang, H.; Liu, Y. F.; Stein, H. S.; Mao, Y. M.; Gao, J. L.; Jiao, M. L.; Dong, Q. et al. High-throughput, combinatorial synthesis of multimetallic nanoclusters. *Proc. Natl. Acad. Sci. USA* **2020**, *117*, 6316–6322.

[13] Pickering, E. J.; Carruthers, A. W.; Barron, P. J.; Middleburgh, S. C.; Armstrong, D. E. J.; Gandy, A. S. High-entropy alloys for advanced nuclear applications. *Entropy* **2021**, *23*, 98.

[14] Löffler, T.; Meyer, H.; Savan, A.; Wilde, P.; Garzón Manjón, A.; Chen, Y. T.; Ventosa, E.; Scheu, C.; Ludwig, A.; Schuhmann, W. Discovery of a multinary noble metal-free oxygen reduction catalyst. *Adv. Energy Mater.* **2018**, *8*, 1802269.

[15] Fang, G.; Gao, J. J.; Lv, J.; Jia, H. L.; Li, H. L.; Liu, W. H.; Xie, G. Q.; Chen, Z. H.; Huang, Y.; Yuan, Q. H. et al. Multi-component nanoporous alloy/(oxy)hydroxide for bifunctional oxygen electrocatalysis and rechargeable Zn-air batteries. *Appl. Catal. B: Environ.* **2020**, *268*, 118431.

[16] Kong, K.; Hyun, J.; Kim, Y.; Kim, W.; Kim, D. Nanoporous structure synthesized by selective phase dissolution of AlCoCrFeNi high entropy alloy and its electrochemical properties as supercapacitor electrode. *J. Power Sources* **2019**, *437*, 226927.

[17] Xu, X.; Du, Y. K.; Wang, C. H.; Guo, Y.; Zou, J. W.; Zhou, K.; Zeng, Z.; Liu, Y. Y.; Li, L. Q. High-entropy alloy nanoparticles on aligned electronspun carbon nanofibers for supercapacitors. *J. Alloys Compd.* **2020**, *822*, 153642.

[18] Ahmad, A. S.; Su, Y.; Liu, S. Y.; Ståhl, K.; Wu, Y. D.; Hui, X. D.; Ruett, U.; Gutowski, O.; Glazyrin, K.; Liermann, H. P. et al. Structural stability of high entropy alloys under pressure and temperature. *J. Appl. Phys.* **2017**, *121*, 235901.

[19] Zaddach, A. J.; Niu, C.; Koch, C. C.; Irving, D. L. Mechanical properties and stacking fault energies of NiFeCrCoMn high-entropy

alloy. *JOM* **2013**, *65*, 1780–1789.
[20] Gludovatz, B.; Hohenwarter, A.; Catoor, D.; Chang, E. H.; George, E. P.; Ritchie, R. O. A fracture-resistant high-entropy alloy for cryogenic applications. *Science* **2014**, *345*, 1153–1158.
[21] Schuh, B.; Mendez-Martin, F.; Völker, B.; George, E. P.; Clemens, H.; Pippan, R.; Hohenwarter, A. Mechanical properties, microstructure and thermal stability of a nanocrystalline CoCrFeMnNi high-entropy alloy after severe plastic deformation. *Acta Mater.* **2015**, *96*, 258–268.
[22] Huang, S.; Li, W.; Lu, S.; Tian, F. Y.; Shen, J.; Holmström, E.; Vitos, L. Temperature dependent stacking fault energy of FeCrCoNiMn high entropy alloy. *Scr. Mater.* **2015**, *108*, 44–47.
[23] Varvenne, C.; Luque, A.; Curtin, W. A. Theory of strengthening in fcc high entropy alloys. *Acta Mater.* **2016**, *118*, 164–176.
[24] Wang, B. F.; Fu, A.; Huang, X. X.; Liu, B.; Liu, Y.; Li, Z. Z.; Zan, X. Mechanical properties and microstructure of the CoCrFeMnNi high entropy alloy under high strain rate compression. *J. Mater. Eng. Perform.* **2016**, *25*, 2985–2992.
[25] Durand, A.; Peng, L.; Laplanche, G.; Morris, J. R.; George, E. P.; Eggeler, G. Interdiffusion in Cr-Fe-Co-Ni medium-entropy alloys. *Intermetallics* **2020**, *122*, 106789.
[26] Luo, H.; Li, Z. M.; Mingers, A. M.; Raabe, D. Corrosion behavior of an equiatomic CoCrFeMnNi high-entropy alloy compared with 304 stainless steel in sulfuric acid solution. *Corros. Sci.* **2018**, *134*, 131–139.
[27] Shi, Y. Z.; Collins, L.; Feng, R.; Zhang, C.; Balke, N.; Liaw, P. K.; Yang, B. Homogenization of $Al_xCoCrFeNi$ high-entropy alloys with improved corrosion resistance. *Corros. Sci.* **2018**, *133*, 120–131.
[28] Zhu, M.; Zhao, B. Z.; Yuan, Y. F.; Guo, S. Y.; Wei, G. Y. Study on corrosion behavior and mechanism of CoCrFeMnNi HEA interfered by AC current in simulated alkaline soil environment. *J. Electroanal. Chem.* **2021**, *882*, 115026.
[29] Zhang, Y. W.; Zhao, S. J.; Weber, W. J.; Nordlund, K.; Granberg, F.; Djurabekova, F. Atomic-level heterogeneity and defect dynamics in concentrated solid-solution alloys. *Curr. Opin. Solid State Mater. Sci.* **2017**, *21*, 221–237.
[30] Bracq, G.; Laurent-Brocq, M.; Perrière, L.; Pirès, R.; Joubert, J. M.; Guillot, I. The fcc solid solution stability in the Co-Cr-Fe-Mn-Ni multi-component system. *Acta Mater.* **2017**, *128*, 327–336.
[31] Laurent-Brocq, M.; Perrière, L.; Pirès, R.; Prima, F.; Vermaut, P.; Champion, Y. From diluted solid solutions to high entropy alloys: On the evolution of properties with composition of multi-components alloys. *Mater. Sci. Eng. A* **2017**, *696*, 228–235.
[32] Wu, Z.; Bei, H.; Otto, F.; Pharr, G. M.; George, E. P. Recovery, recrystallization, grain growth and phase stability of a family of FCC-structured multi-component equiatomic solid solution alloys. *Intermetallics* **2014**, *46*, 131–140.
[33] Billington, D.; James, A. D. N.; Harris-Lee, E. I.; Lagos, D. A.; O' Neill, D.; Tsuda, N.; Toyoki, K.; Kotani, Y.; Nakamura, T.; Bei, H. et al. Bulk and element-specific magnetism of medium-entropy and high-entropy Cantor-Wu alloys. *Phys. Rev. B* **2020**, *102*, 174405.
[34] Kao, Y. F.; Chen, S. K.; Chen, T. J.; Chu, P. C.; Yeh, J. W.; Lin, S. J. Electrical, magnetic, and Hall properties of $Al_xCoCrFeNi$ high-entropy alloys. *J. Alloys Compd.* **2011**, *509*, 1607–1614.
[35] Jasiewicz, K.; Cieslak, J.; Kaprzyk, S.; Tobola, J. Relative crystal stability of $Al_xFeNiCrCo$ high entropy alloys from XRD analysis and formation energy calculation. *J. Alloys Compd.* **2015**, *648*, 307–312.
[36] Yusenko, K. V.; Riva, S.; Crichton, W. A.; Spektor, K.; Bykova, E.; Pakhomova, A.; Tudball, A.; Kupenko, I.; Rohrbach, A.; Klemme, S. et al. High-pressure high-temperature tailoring of high entropy alloys for extreme environments. *J. Alloys Compd.* **2018**, *738*, 491–500.
[37] Smekhova, A.; Kuzmin, A.; Siemensmeyer, K.; Luo, C.; Chen, K.; Radu, F.; Weschke, E.; Reinholz, U.; Buzanich, A. G.; Yusenko, K. V. Al-driven peculiarities of local coordination and magnetic properties in single-phase Al_x-CrFeCoNi high-entropy alloys. *Nano Res.* **2022**, *15*, 4845–4858.
[38] Čižek, L.; Kratochvíl, P.; Smola, B. Solid solution hardening of copper crystals. *J. Mater. Sci.* **1974**, *9*, 1517–1520.
[39] Gypen, L. A.; Deruyttere, A. Multi-component solid solution hardening. *J. Mater. Sci.* **1977**, *12*, 1028–1033.
[40] Ma, D. C.; Grabowski, B.; Körmann, F.; Neugebauer, J.; Raabe, D. *Ab initio* thermodynamics of the CoCrFeMnNi high entropy alloy: Importance of entropy contributions beyond the configurational one. *Acta Mater.* **2015**, *100*, 90–97.
[41] Tong, Y. ; Velisa, G. ; Yang, T. ; Jin, K. ; Lu, C. ; Bei, H. ; Ko, J. Y. P. ; Pagan, D. C. ; Huang, R. ; Zhang, Y. et al. Probing local lattice distortion in medium- and high-entropy alloys. 2017, arXiv:1707.07745. arXiv.org e-Print archive. https://arxiv.org/abs/1707.07745 (accessed Apr 1, 2022).
[42] Okamoto, N. L.; Yuge, K.; Tanaka, K.; Inui, H.; George, E. P. Atomic displacement in the CrMnFeCoNi high-entropy alloy—A scaling factor to predict solid solution strengthening. *AIP Adv.* **2016**, *6*, 125008.
[43] Zhang, F. X.; Tong, Y.; Jin, K.; Bei, H. B.; Weber, W. J.; Huq, A.; Lanzirotti, A.; Newville, M.; Pagan, D. C.; Ko, J. Y. P. et al. Chemical complexity induced local structural distortion in NiCoFeMnCr high-entropy alloy. *Mater. Res. Lett.* **2018**, *6*, 450–455.
[44] Ding, Q. Q.; Zhang, Y.; Chen, X.; Fu, X. Q.; Chen, D. K.; Chen, S. J.; Gu, L.; Wei, F.; Bei, H. B.; Gao, Y. F. et al. Tuning element distribution, structure and properties by composition in high-entropy alloys. *Nature* **2019**, *574*, 223–227.
[45] Cantor, B. Multicomponent high-entropy Cantor alloys. *Prog. Mater. Sci.* **2021**, *120*, 100754.
[46] Oh, H. S.; Odbadrakh, K.; Ikeda, Y.; Mu, S.; Körmann, F.; Sun, C. J.; Ahn, H. S.; Yoon, K. N.; Ma, D. C.; Tasan, C. C. et al. Element-resolved local lattice distortion in complex concentrated alloys: An observable signature of electronic effects. *Acta Mater.* **2021**, *216*, 117135.
[47] Guo, S.; Ng, C.; Lu, J.; Liu, C. T. Effect of valence electron concentration on stability of fcc or bcc phase in high entropy alloys. *J. Appl. Phys.* **2011**, *109*, 103505.
[48] Zhang, R. P.; Zhao, S. T.; Ding, J.; Chong, Y.; Jia, T.; Ophus, C.; Asta, M.; Ritchie, R. O.; Minor, A. M. Short-range order and its impact on the CrCoNi medium-entropy alloy. *Nature* **2020**, *581*, 283–287.
[49] He, Q. F.; Tang, P. H.; Chen, H. A.; Lan, S.; Wang, J. G.; Luan, J. H.; Du, M.; Liu, Y.; Liu, C. T.; Pao, C. W. et al. Understanding chemical short-range ordering/demixing coupled with lattice distortion in solid solution high entropy alloys. *Acta Mater.* **2021**, *216*, 117140.
[50] Oh, H. S.; Ma, D. C.; Leyson, G. P.; Grabowski, B.; Park, E. S.; Körmann, F.; Raabe, D. Lattice distortions in the FeCoNiCrMn high entropy alloy studied by theory and experiment. *Entropy* **2016**, *18*, 321.
[51] Smekhova, A.; Kuzmin, A.; Siemensmeyer, K.; Abrudan, R.; Reinholz, U.; Buzanich, A. G.; Schneider, M.; Laplanche, G.; Yusenko, K. V. Inner relaxations in equiatomic single-phase high-entropy cantor alloy. *J. Alloys Compd.* **2022**, *920*, 165999.
[52] Fantin, A.; Lepore, G. O.; Manzoni, A. M.; Kasatikov, S.; Scherb, T.; Huthwelker, T.; d'Acapito, F.; Schumacher, G. Short-range chemical order and local lattice distortion in a compositionally complex alloy. *Acta Mater.* **2020**, *193*, 329–337.
[53] Schneeweiss, O.; Friák, M.; Dudová, M.; Holec, D.; Šob, M.; Kriegner, D.; Holý, V.; Beran, P.; George, E. P.; Neugebauer, J. et al. Magnetic properties of the CrMnFeCoNi high-entropy alloy. *Phys. Rev. B* **2017**, *96*, 014437.
[54] Sarkar, A.; Eggert, B.; Witte, R.; Lill, J.; Velasco, L.; Wang, Q. S.; Sonar, J.; Ollefs, K.; Bhattacharya, S. S.; Brand, R. A. et al. Comprehensive investigation of crystallographic, spin-electronic and magnetic structure of $(Co_{0.2}Cr_{0.2}Fe_{0.2}Mn_{0.2}Ni_{0.2})_3O_4$: Unraveling the suppression of configuration entropy in high entropy oxides. *Acta Mater.* **2022**, *226*, 117581.
[55] Timoshenko, J.; Keller, K. R.; Frenkel, A. I. Determination of bimetallic architectures in nanometer-scale catalysts by combining molecular dynamics simulations with X-ray absorption spectroscopy. *J. Chem. Phys.* **2017**, *146*, 114201.
[56] Timoshenko, J.; Jeon, H. S.; Sinev, I.; Haase, F. T.; Herzog, A.; Roldan Cuenya, B. Linking the evolution of catalytic properties and structural changes in copper-zinc nanocatalysts using *operando*

EXAFS and neural-networks. *Chem. Sci.* **2020**, *11*, 3727–3736.
[57] Stöhr, J.; Siegmann, H. C. *Magnetism*: *From Fundamentals to Nanoscale Dynamics*; Springer: Berlin, 2006.
[58] Lucas, M. S.; Mauger, L.; Muñoz, J. A.; Xiao, Y. M.; Sheets, A. O.; Semiatin, S. L.; Horwath, J.; Turgut, Z. Magnetic and vibrational properties of high-entropy alloys. *J. Appl. Phys.* **2011**, *109*, 07E307.
[59] Körmann, F.; Ma, D.; Belyea, D. D.; Lucas, M. S.; Miller, C. W.; Grabowski, B.; Sluiter, M. H. F. "Treasure maps" for magnetic high-entropy-alloys from theory and experiment. *Appl. Phys. Lett.* **2015**, *107*, 142404.
[60] Riesemeier, H.; Ecker, K.; Görner, W.; Müller, B. R.; Radtke, M.; Krumrey, M. Layout and first XRF applications of the BAM*line* at BESSY II. *X-Ray Spectrom.* **2005**, *34*, 160–163.
[61] Lutz, C.; Hampel, S.; Ke, X.; Beuermann, S.; Turek, T.; Kunz, U.; Guilherme Buzanich, A.; Radtke, M.; Fittschen, U. E. A. Evidence for redox reactions during vanadium crossover inside the nanoscopic water-body of Nafion 117 using X-ray absorption near edge structure spectroscopy. *J. Power Sources* **2021**, *483*, 229176.
[62] Timoshenko, J.; Kuzmin, A.; Purans, J. Reverse Monte Carlo modeling of thermal disorder in crystalline materials from EXAFS spectra. *Comput. Phys. Commun.* **2012**, *183*, 1237–1245.
[63] Timoshenko, J.; Kuzmin, A.; Purans, J. EXAFS study of hydrogen intercalation into ReO_3 using the evolutionary algorithm. *J. Phys. Condens. Matter* **2014**, *26*, 055401.
[64] Timoshenko, J.; Kuzmin, A. Wavelet data analysis of EXAFS spectra. *Comput. Phys. Commun.* **2009**, *180*, 920–925.
[65] Kuzmin, A.; Chaboy, J. EXAFS and XANES analysis of oxides at the nanoscale. *IUCrJ* **2014**, *1*, 571–589.
[66] XAESA, v0.06; GitHub: 2022 [Online]. https://github.com/aklnk/xaesa (accessed Nov 1, 2020).
[67] Ankudinov, A. L.; Ravel, B.; Rehr, J. J.; Conradson, S. D. Real space multiple-scattering calculation and interpretation of X-ray absorption near-edge structure. *Phys. Rev. B* **1998**, *58*, 7565–7576.
[68] Rehr, J. J.; Albers, R. C. Theoretical approaches to X-ray absorption fine structure. *Rev. Mod. Phys.* **2000**, *72*, 621–654.
[69] Englisch, U.; Rossner, H.; Maletta, H.; Bahrdt, J.; Sasaki, S.; Senf, F.; Sawhney, K. J. S.; Gudat, W. The elliptical undulator UE46 and its monochromator beam-line for structural research on nanomagnets at BESSY-II. *Nucl. Instrum. Methods Phys. Res. A: Accel. Spectrom. Detect. Assoc. Equip.* **2001**, *467–468*, 541–544.
[70] Schmitz, D.; Rossner, H.; Imperia, P.; Maletta, H.; Bahrdt, J.; Follath, R.; Frentrup, W.; Gaupp, A.; Holldack, K.; Mertins, H. C. et al. Commissioning results of the UE46-PGM beamline. *BESSY Annual Report.* **2002**, 358–361.
[71] Noll, T.; Radu, F. The mechanics of the vekmag experiment. In *Proceedings of the 9th Mechanical Engineering Design of Synchrotron Radiation Equipment and Instrumentation* (*MEDSI'16*), Barcelona, Spain, 2017, pp 370–373.
[72] Li, Y. J.; Kostka, A.; Savan, A.; Ludwig, A. Atomic-scale investigation of fast oxidation kinetics of nanocrystalline CrMnFeCoNi thin films. *J. Alloys Compd.* **2018**, *766*, 1080–1085.
[73] Hobbs, D.; Hafner, J.; Spišák, D. Understanding the complex metallic element Mn. I. Crystalline and noncollinear magnetic structure of α-Mn. *Phys. Rev. B* **2003**, *68*, 014407.
[74] Niu, C.; Zaddach, A. J.; Oni, A. A.; Sang, X.; Hurt III, J. W.; LeBeau, J. M.; Koch, C. C.; Irving, D. L. Spin-driven ordering of Cr in the equiatomic high entropy alloy NiFeCrCo. *Appl. Phys. Lett.* **2015**, *106*, 161906.
[75] Lee, C. H.; Chin, H. H.; Zeng, K. Y.; Chang, Y. J.; Yeh, A. C.; Yeh, J. W.; Lin, S. J.; Wang, C. C.; Glatzel, U.; Huang, E. W. Tailoring ferrimagnetic transition temperatures, coercivity fields, and saturation magnetization by modulating Mn concentration in $(CoCrFeNi)_{1-x}Mn_x$ high-entropy alloys. *Front. Mater.* **2022**, *9*, 824285.
[76] Nascimento, C. B.; Donatus, U.; Ríos, C. T.; Antunes, R. A. Electronic properties of the passive films formed on CoCrFeNi and CoCrFeNiAl high entropy alloys in sodium chloride solution. *J. Mater. Res. Technol.* **2020**, *9*, 13879–13892.
[77] Shi, Y. Z.; Yang, B.; Rack, P. D.; Guo, S. F.; Liaw, P. K.; Zhao, Y. High-throughput synthesis and corrosion behavior of sputter-deposited nanocrystalline $Al_x(CoCrFeNi)_{100-x}$ combinatorial high-entropy alloys. *Mater. Des.* **2020**, *195*, 109018.
[78] Mitra, C.; Hu, Z.; Raychaudhuri, P.; Wirth, S.; Csiszar, S. I.; Hsieh, H. H.; Lin, H. J.; Chen, C. T.; Tjeng, L. H. Direct observation of electron doping in $La_{0.7}Ce_{0.3}MnO_3$ using X-ray absorption spectroscopy. *Phys. Rev. B* **2003**, *67*, 092404.
[79] Cramer, S. P.; DeGroot, F. M. F.; Ma, Y.; Chen, C. T.; Sette, F.; Kipke, C. A.; Eichhorn, D. M.; Chan, M. K.; Armstrong, W. H.; Libby, E. et al. Ligand field strengths and oxidation states from manganese L-edge spectroscopy. *J. Am. Chem. Soc.* **1991**, *113*, 7937–7940.
[80] Thole, B. T.; Carra, P.; Sette, F.; van der Laan, G. X-ray circular dichroism as a probe of orbital magnetization. *Phys. Rev. Lett.* **1992**, *68*, 1943–1946.
[81] Carra, P.; Thole, B. T.; Altarelli, M.; Wang, X. D. X-ray circular dichroism and local magnetic fields. *Phys. Rev. Lett.* **1993**, *70*, 694–697.
[82] Mu, S.; Samolyuk, G. D.; Wimmer, S.; Troparevsky, M. C.; Khan, S. N.; Mankovsky, S.; Ebert, H.; Stocks, G. M. Uncovering electron scattering mechanisms in NiFeCoCrMn derived concentrated solid solution and high entropy alloys. *npj Comput. Mater.* **2019**, *5*, 1.
[83] Scherz, A. Spin-dependent X-ray absorption spectroscopy of 3d transition metals: Systematics and applications. Ph.D. Dissertation, Freie University Berlin, Berlin, Germany, 2003.
[84] Jin, K.; Sales, B. C.; Stocks, G. M.; Samolyuk, G. D.; Daene, M.; Weber, W. J.; Zhang, Y.; Bei, H. Tailoring the physical properties of Ni-based single-phase equiatomic alloys by modifying the chemical complexity. *Sci. Rep.* **2016**, *6*, 20159.